Check for updates

O$_2$-tolerant CO dehydrogenase via tunnel redesign for the removal of CO from industrial flue gas

Suk Min Kim [1,4], Jinhee Lee [1,4], Sung Heuck Kang [1,2,4], Yoonyoung Heo [3,4], Hye-Jin Yoon[3], Ji-Sook Hahn[2], Hyung Ho Lee [3,5 ✉] and Yong Hwan Kim [1,5 ✉]

Ni–Fe carbon monoxide dehydrogenases (CODHs) are nearly diffusion-limited biocatalysts that oxidize CO. Their O$_2$ sensitivity, however, is a major drawback for industrial applications. Here we compare the structures of a fast CODH with a high O$_2$ sensitivity (ChCODH-II) and a slower CODH with a lower O$_2$ sensitivity (ChCODH-IV) (Ch, Carboxydothermus hydrogenoformans). Some variants obtained by simple point mutations of the bottleneck residue (A559) in the gas tunnel showed 61–148-fold decreases in O$_2$ sensitivity while maintaining high turnover rates. The variant structure A559W showed obstruction of one gas tunnel, and molecular dynamics supported the locked position of the mutated side chain in the tunnel. The variant was exposed to different gas mixtures, from simple synthetic gas to sophisticated real flue from a steel mill. Its catalytic properties remained unchanged, even at high O$_2$ levels, and the efficiency was maintained for multiple cycles of CO detoxification/regeneration.

arge amounts of carbon monoxide (CO) are emitted from both natural sources and human activity[1] (for example, annually over 21.9 billion Nm^3 of CO-containing flue gases from the South Korean steelmaking company POSCO)[2,3]. CO, the most abundant air pollutant found in the atmosphere other than CO$_2$, according to the Organisation for Economic Co-operation and Development database (https://data.oecd.org/air/air-and-ghg-emissions.htm#indicator-chart, air emissions source in 2017), can provide sufficient carbon and energy for converting waste gas into fuels and chemicals through a clean and sustainable method. One of the most ideal ways to convert inexpensive, abundant and recyclable CO$_2$ into fuels and chemicals is the employment of carbon monoxide dehydrogenases (CODHs) capable of oxidizing CO to give CO$_2$ in the manner of bacteria and archaea[4]. Practical applications of these CODHs, which show remarkable substrate selectivity and viability in gas mixtures even with metal-catalyst inhibitors (sulfur compounds, aromatics, halogens, tar and potentially reactive nitrogen species)[5–8], are promising; however, they remain very limited due to the diminished activity of CODHs[2] in the presence of atmospheric oxygen (O$_2$).

The two CODH families are classified by the metal species of the active site[2,9,10], namely, Mo–Cu CODHs with a dinuclear [(CuSMo(O)O) and (CuSMo(O)OH$_2$)] (ref. [11]) cluster (EC 1.2.5.3) and Ni–Fe CODHs with a distinctive [NiFe$_3$S$_4$OH$_x$] cluster (EC 1.2.7.4); these catalyse a moderate rate of aerobic CO conversion (93.3 s^{-1}) (ref. [12]) or a very high rate of anaerobic CO conversion (31,000 s^{-1}) (ref. [13]), respectively. Unlike the highly O$_2$-sensitive CODHs, two Ni–Fe CODHs from Carboxydothermus hydrogenoformans (ChCODH-IV)[9] and Desulfovibrio vulgaris (DvCODH)[14] that are less O$_2$ sensitive show unique features and provide intriguing insights into how the active-site environment is changed by O$_2$ exposure. For the effective and widespread use of CODHs in industrial fields, the inevitable disadvantage of a poor activity under aerobic conditions must be overcome. This barrier motivated us to address the issue of the O$_2$ sensitivity of ChCODH-II, which has the

highest known CO oxidation rate (31,000 s^{-1}) (ref. [13]), for practical applications in treating pollutant CO flue gases.

Here we demonstrate a substrate tunnel modification of ChCODH-II using a rational approach based on protein sequences and structures from Ni–Fe CODHs, which leads to greatly decreased O$_2$ sensitivity of the enzyme during oxidation of CO to give CO$_2$. By analysing substrate tunnels close to the active site (C cluster) of ChCODH-II, we discovered a common bottleneck of substrate tunnels in Ni–Fe CODHs, which included acetyl-CoA synthase–CODH complexes involved in the Wood–Ljungdahl pathway. Our mutation and kinetic experiments revealed that under near-atmospheric conditions, the redesigned ChCODH-II variants achieved approximately 100-fold decreases in O$_2$ sensitivity relative to that of the ChCODH-II wild type (WT) while maintaining excellent catalytic performances. In addition, the CO of real industrial flue gas was completely removed by the engineered enzymes even under atmospheric O$_2$ conditions, which strongly indicates the potential for application as a CO-removal biocatalyst in industrial fields[2,3].

Results

A bottleneck for the O$_2$ response in ChCODHs. To explore key regions for O$_2$ sensitivity in Ni–Fe CODHs, we compared the protein sequences and analysed the phylogenetic trees of O$_2$-sensitive ChCODH-II and the less O$_2$-sensitive ChCODH-IV with five forms (ChCODH I–V) as the genomic context[15] (Fig. 1a,b and Supplementary Fig. 1). Five residues (D94, E101, R187, Y558 and Q559) of ChCODH-IV are quite different from those of ChCODH-II. These residues are conserved in DvCODH. Moreover, analysis of the structures and gas tunnels in Ni–Fe CODHs suggests that of the two residues Y558 and Q559 located along the tunnel, only Y558 is predicted to participate in gas substrate transport in the less O$_2$-sensitive ChCODH-IV (Fig. 1c and Supplementary Fig. 2). In O$_2$-sensitive ChCODH-II, the corresponding residues A559 and M560 are positioned similarly (Supplementary Fig. 2). Similar to Y558 in ChCODH-IV, the side chain of the tunnel-forming
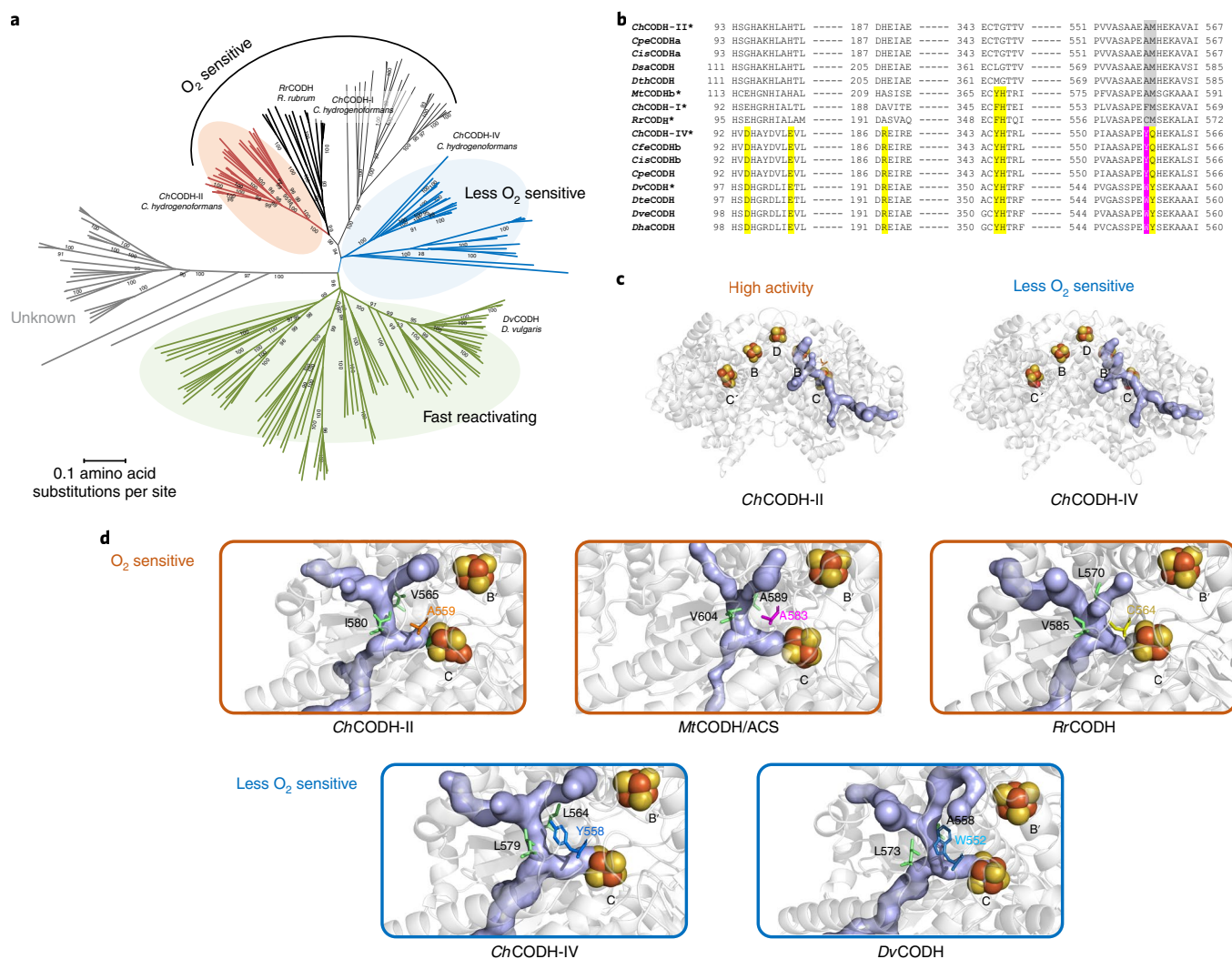
Fig. 1 | Discovery of the bottleneck for the O₂ response in Ni–Fe CODHs. a, Phylogenetic tree of *Ch*CODHs. Through phylogenetic analysis of Ni–Fe CODH proteins, we found that at least two different clades, those that contained *Ch*CODH-IV and *Dv*CODH, are closely localized, distinct from the common lineage and are assumed to be insensitive to and possess unique mechanisms against molecular O₂. The phylogenetic trees showed orthologous relationships based on the amino acid sequences of the CODH proteins (see Methods for details). **b**, Partial sequence alignment of CODH proteins. Five residues (D94, E101, R187 and Q559 with a yellow shade and Y558 with a pink shade) are conserved in *Ch*CODH-IV and *Dv*CODH but are quite different to those of *Ch*CODH-II. Information on the protein names, including the characterized CODHs with an asterisk and associated non-redundant protein accession numbers, is given in Supplementary Fig. 1. **c**, Gas tunnels identified in the *Ch*CODH-II and *Ch*CODH-IV structures. *Ch*CODH-II (PDB 1SU7) shows the highest activity towards CO but is more sensitive to O₂ than *Ch*CODH-IV (PDB 6ELQ). The homodimeric *Ch*CODH-II and *Ch*CODH-IV contain five metal clusters: the [NiFe₃S₄] cluster at the catalytic site (C cluster), the [Fe₄S₄] cubane-type cluster (B cluster) and the [Fe₄S₄] cluster in the dimer interface (D cluster), which is unlike the [Fe₂S₂] D cluster in *Dv*CODH, implying that the catalytic mechanisms of *Ch*CODHs are similar due to the identical metal cluster contents. **d**, Common bottleneck points of gas tunnels near the active site of Ni–Fe CODHs. A branch of the gas tunnels depicted in the panels ends at cluster C directly above the apical coordination site of the Ni atom. In the structure of *Ch*CODH-II, the gas tunnels and the triad residues (A559, V565 and I580) that constitute the bottleneck are indicated. In less O₂-sensitive CODHs, the residues that correspond to A559 of *Ch*CODH-II are bulky residues, such as tryptophan and tyrosine. However, the corresponding side chains in the O₂-sensitive CODHs are relatively small. *Rr, Rhodospirillum rubrum*.

A559 was also oriented towards the substrate tunnel, whereas the side chain of M560 faced away from the tunnel.

In addition, we realized that residue A559 forms a triad with its neighbouring residues (V565 and I580) along the junction of the substrate tunnels (Fig. 1d). Interestingly, the substrate tunnels with triad residues appear to be non-selective paths where water molecules and xenon-coordinating residues coexist (Supplementary Fig. 3). This suggests that various molecules (which include water, CO and O₂) can access the active site through putatively non-selective substrate tunnels. Much to our surprise, the triad near the active site is

universal in structurally similar Ni–Fe CODHs, even in the different bifunctional acetyl-CoA synthase–*Mt*CODH (*Mt, Moorella thermoacetica*) subunit (Supplementary Table 1). Moreover, this narrowest position at the conserved triad is likely to act as a bottleneck in gas tunnels that critically affects the transport rate of substrates depending on the tunnel characteristics, such as diameter and dynamic fluctuation[16] (Supplementary Fig. 4a,b). We therefore hypothesized that the selective obstruction of the common bottleneck point in the gas tunnel would decrease the O₂ sensitivity of CODH by blocking O₂ transfer into the active site of the C- cluster. Accordingly, by
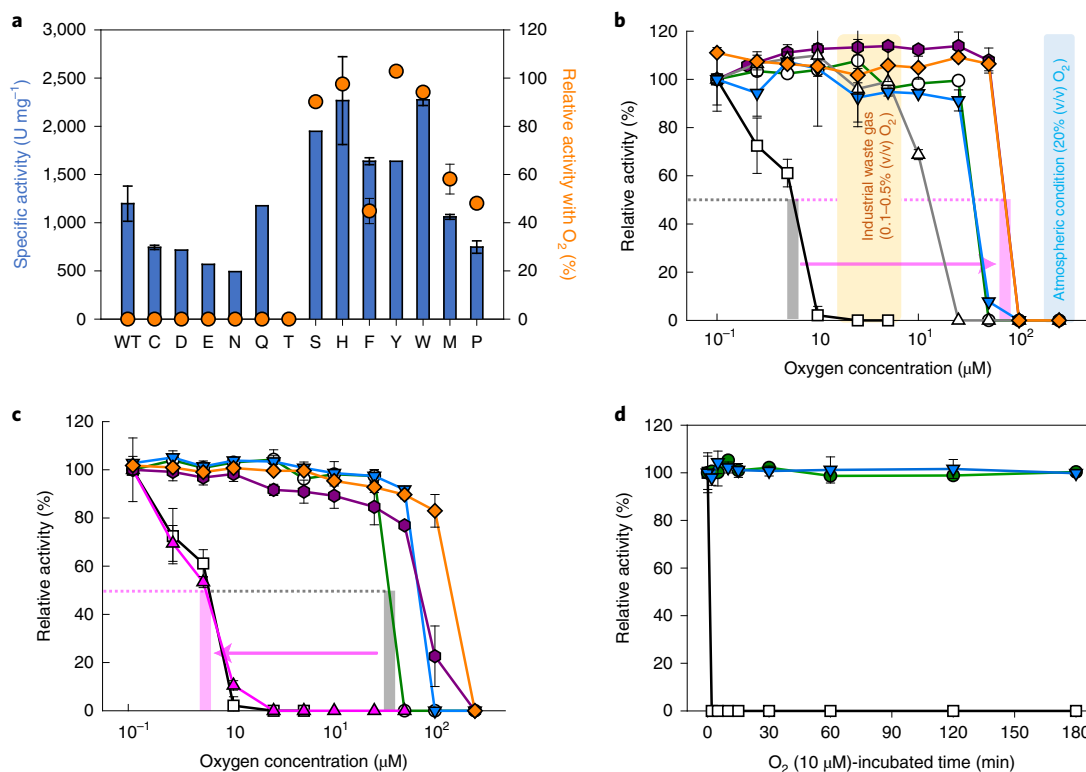
Fig. 2 | O₂ sensitivity of Ni–Fe CODHs and its variants. a, Specific activities of A559X variants and relative activities with O_2. CO oxidation catalysed by *Ch*CODH-II variants in the absence (blue) or presence (orange) of O_2. The data represent the mean ± s.d., as determined from three independent experiments. See the detailed conditions and abbreviations in Supplementary Fig. 5. **b,** Decreased O_2 sensitivity of Ni–Fe CODHs and its variants. The effect of the O_2 concentration on Ni–Fe CODHs (open symbols) and engineered *Ch*CODHs (closed symbols) was observed for *Ch*CODH-II (squares), *Ch*CODH-IV (circles), *Dv*CODH (triangles), *Ch*CODH-II A559H (diamonds), A559S (hexagons) and A559W (reverse triangles). The grey and pink bars indicate the half-maximal inhibitory O_2 concentrations of *Ch*CODH-II WT and A559H, respectively. The horizontal arrow shows the increase in the half-maximal inhibitory O_2 concentration from *Ch*CODH-II to A559H. The data represent the mean ± s.d., as determined from $n = 3$ independent experiments (Methods). **c,** Changes in O_2 sensitivity in *Ch*CODH-IV and its variants. The effect of the O_2 concentration on *Ch*CODH-IV (open symbols) and its variants (closed symbols) was measured for *Ch*CODH-II (squares), *Ch*CODH-IV (circles), *Ch*CODH-IV Y558A (triangles), Y558H (diamonds), Y558S (hexagons) and Y558W (reverse triangles). No activity was observed for *Ch*CODH-IV Y558S or *Dv*CODH W552A. The grey and pink bars indicate the half-maximal O_2 concentrations of *Ch*CODH-IV WT and Y558A, respectively. The horizontal arrow shows the decrease in the half-maximal inhibitory O_2 concentration from *Ch*CODH-IV to Y558A. The data represent the mean ± s.d., as determined from $n = 3$ independent experiments. **d,** Time course of O_2 influence on *Ch*CODHs. The residual activities of *Ch*CODH-II (squares), A559W (reverse triangles) and *Ch*CODH-IV (circles) in the presence of 10 μM O_2 were monitored for 3 h. The data represent the mean ± s.d., as determined from $n = 3$ independent experiments.

substituting amino acids and experimentally demonstrating decreased O_2 sensitivity, we designed a number of variants displaying different characteristics at the bottleneck point. The results illuminate the relationships between tunnel characteristics and the O_2 sensitivity of CODH- or CODH-harbouring cells.

O_2 sensitivity and catalytic properties of *Ch*CODH variants. First, to determine the respective effects of bulk, charge, polarity and hydrophobicity at the putative key positions 559 and/or 560, 565 and 580 of *Ch*CODH-II, we constructed and purified a number of single and double variants in *Escherichia coli* (Supplementary Table 2 and Supplementary Fig. 5). The variants were screened based on their specific activities of CO oxidation and their residual activities after O_2 exposure (Supplementary Table 3). The effects of the mutations showed a simple and clear correlation between the aromatic side chains and decreased O_2 sensitivity, except for A559S (Fig. 2a). After exposure to dissolved O_2 (10 μM), the residual activities of the variants with aromatic groups, A559H, A559W, A559Y (>90%), A559F and A559P (40–50%), sulfur-containing A559M (58%) and hydroxyl-containing A559S (90%) were detected, whereas *Ch*CODH-II WT exhibited zero residual activity, which shows a

complete loss of activity. Additionally, compared with that of WT, the specific activities of A559F, A559H, A559S, A559W and A559Y for the substrate CO were increased by approximately 1.38–2.5-fold (Supplementary Table 3). The amino acid side chains at the 559 position seemed to have a strong impact on the O_2 sensitivity and CO oxidation in *Ch*CODH-II.

Figure 2b demonstrates the remarkable effects of mutations to bulkier amino acids on improving the resistance to O_2. The engineered A559W and A559H *Ch*CODH-II showed an over 50% residual activity due to the notably lower O_2 sensitivity, even in the presence of 38.2–92.9 μM O_2, whereas the WT showed only a 50% residual activity at 0.63 μM O_2, which suggested an approximately 60.6–147.5-fold improvement in the half-maximal inhibitory O_2 concentration (Supplementary Table 4). The O_2 sensitivity of the engineered variant of *Ch*CODH-II was much lower than those of the naturally less O_2-sensitive *Ch*CODH-IV and *Dv*CODH, which would enable its application to industrial flue gas that contains 1.5–6.5 μM O_2 (0.1–0.5%). Table 1 indicates that most *Ch*CODH-II variants have high catalytic rates ($k_{cat} \approx 2,000 \, s^{-1}$ at 30 °C) similar to the value ($k_{cat} \approx 1,500 \, s^{-1}$ at 20 °C) reported by Ragsdale and co-workers[17], which suggests that the engineering of enzymes did

Table 1 | Catalytic properties of ChCODH variants

CODH, variant	Substrate	Specific activity[a] (U mg^{-1})	$K_{M,app}$ (mM)[b]	$k_{cat,app}$ (s^{-1})[c]	$k_{cat,app}/K_{M,app}$ (s^{-1} mM^{-1})	$K_{I,app}^{O_2}$ [d]	$K_{M,app}/K_{I,app}^{O_2}$
ChCODH-II	CO	1,300±108.5	0.020±0.002	1,500±67.0	75,800±3,840	0.012±0.001	1,600±45.2
	EV	900±28.2	1.8±0.1	1,000±15.7	560±15.1		
A559H	CO	2,100±118.0	0.061±0.002	2,300±37.8	37,000±991	5.4±0.8	11.5±1.2
	EV	1,900±63.5	2.1±0.1	2,300±71.9	1,100±22.9		
A559S	CO	1,900±57.6	0.041±0.003	2,000±61.6	50,000±2,790	2.9±0.8	14.6±2.9
	EV	2,200±53.5	2.1±0.1	2,600±98.2	1,200±37.0		
A559Y	CO	2,000±118.8	0.024±0.004	1,500±78.1	62,000±8,360	0.6±0.1	38.8±0.1
	EV	1,700±62.8	1.9±0.1	1,800±75.6	1,100±19.3		
A559W	CO	1,800±111.0	0.034±0.002	1,800±49.5	53,000±2,300	1.2±0.1	27.1±0.7
	EV	2,000±13.2	2.0±0.1	2,100±38.8	1,000±40.4		
ChCODH-IV	EV	85±1.2	1.3±0.1	87±0.3	67±2.1	ND	ND
Y558A	EV	68±0.4	1.1±0.1	63±0.1	57±0.7	ND	ND
Y558H	EV	85±3.8	0.9±0.1	86±0.1	99±2.8	ND	ND
Y558S	EV	36±2.2	1.4±0.1	34±1.4	25±2.7	ND	ND
Y558W	EV	99±0.5	1.1±0.1	110±1.4	100±2.4	ND	ND

[a]Specific activities were determined at 20 mM ethyl viologen (EV) in the presence of HEPES buffer saturated with CO (30 °C, pH 8). Values are the means±standard variation, $n=3$. [b]Kinetic data were assayed at 30 °C, pH 8. The kinetic parameters were calculated by fitting the initial rates obtained at seven different EV concentrations (0.5–8 mM) and five different CO concentrations (0.01–0.16 mM) to the Hanes–Woolf equation using SigmaPlot 10.0. All the enzymatic activities were determined in triplicate (see details in Methods). [c]The values of $k_{cat,app}$ were calculated from V_{max} for EV and V_{max} for CO. [d]For K_I determination, half-maximal inhibitory (IC$_{50}$) O$_2$ concentration values were calculated using nonlinear regressions (four-parameter logistic curve). Subsequent K_I values were calculated using the Cheng–Prusoff equation (equation (1))[30]. ND, not determined.

not disturb the catalytic activity. Moreover, the ChCODH-II variants were as robust as the WT enzyme up to 70 °C (Supplementary Table 5), which presents the additional advantage of higher activities and stabilities even at relatively high temperatures.

Regarding the catalytic properties with CO as a substrate, the apparent Michaelis constant ($K_{M,app}$) for CO in ChCODH-II WT was estimated to be 20 μM, which is slightly higher than the value of 8 μM reported by Dobbek and co-workers[9], but is similar to the value of 18 μM reported by Meyer and co-workers[13]. For the variants, the $K_{M,app}$ value of 24 μM CO for A559Y showed a very similar CO affinity to that of the WT (20 μM), whereas other mutants exhibited a slightly decreased CO affinity. Often, mutations that show a decreased O$_2$ binding exhibit a corresponding decrease in substrate binding (for example, RuBisCo (ref. [18])). Owing to the possibility of competition between CO and O$_2$ for the variants, we determined the ratio $K_{M,app}^{CO}/K_{I,app}^{O_2}$ ($K_{I,app}$, inhibition constant), which is crucial to evaluate the efficiency of the variants. Compared with the WT, the variants showed 41–139-fold increases in the relative affinities for CO over O$_2$, which indicates that these variants are highly selective for CO even in the presence of O$_2$. However, changing the flexibility at the bottleneck of the tunnel will alter catalytic parameters, such as $K_{M,app}$ for CO. In addition, it may be that a small portion of the substrate CO can be transferred by the mutated tunnel, but most of the CO transfer takes place through other tunnels, as shown in Supplementary Fig. 3. A slightly higher K_M value for CO implies a lowered affinity of the mutant for CO due to a decreased flexibility at the bottleneck or the possibility of less CO being transferred through this engineered tunnel to bind the active site.

In contrast, mutating the other two residues in the junction triad, V565 and I580, did not decrease O$_2$ sensitivity, which indicates that the A559 position is a key site for O$_2$ access in ChCODH-II (Supplementary Table 3). Moreover, among the mutations of M560, another unique position in ChCODH-II and IV, the M560Q variant, showed only a slightly lower O$_2$ sensitivity (Supplementary Fig. 5), which suggests that this site is not crucial for decreasing O$_2$ sensitivity.

As shown in Fig. 2c, in ChCODH-IV, we examined the reverse of the changes that decreased the O$_2$ sensitivity of ChCODH-II and Y558A to reconfirm the results for the ChCODH-II variants. As expected, Y558A was very sensitive to O$_2$, in fact, as sensitive as ChCODH-II, which thus indicates that the role of Y558 (ChCODH-IV) is similar to that in the engineered A559 mutants (ChCODH-II) as a key site for decreased O$_2$ sensitivity. This supported the hypothesis that the substitution of tyrosine for alanine decreases O$_2$ sensitivity but does not change the catalytic properties of Y558A relative to those of ChCODH-IV WT (Table 1). With reference to the data on the reduced O$_2$ sensitivities of the ChCODH-II variants, positive mutations (tryptophan and histidine) were introduced at Y558, and the residual activities of the ChCODH-IV variants were observed (Fig. 2c). These results showed that replacing tyrosine with tryptophan or histidine at 558 also decreased the O$_2$ sensitivity in ChCODH-IV, as is the case for the ChCODH-II A559 variants. Consequently, we concluded that the 559 or 558 position in either ChCODH-II or IV was the commonly shared key site that affected O$_2$ sensitivity.

For the stable and efficient conversion of CO in the presence of O$_2$, we further estimated the stability of engineered A559W as an oxidizing biocatalyst (Fig. 2d). At 10 μM O$_2$, the relative activities of ChCODH-IV and A559W of ChCODH-II were stably maintained over time, but the activity of ChCODH-II WT rapidly diminished. These results revealed that the variant A559W exhibited a stable activity at 10 μM O$_2$ despite the rapid O$_2$ inactivation of ChCODH-II WT and the low CO conversion of ChCODH-IV. It is well-known that most Ni–Fe CODHs are inactivated by O$_2$ within only a few minutes[13,14], and inactivation is more severe in the absence of O$_2$ scavengers, such as dithiothreitol (DTT) and dithioerythritol (DTE)[19]. Furthermore, variants exposed to O$_2$ for several hours can efficiently undergo CO conversion at higher conversion rates than can ChCODH-IV, which has a low specific activity (~90 U mg^{-1}). Therefore, it is predicted that low O$_2$-sensitive ChCODH-II variants will provide a good performance in removing CO from industrial waste gas mixtures that contain O$_2$.

Structural analysis of less O$_2$-sensitive ChCODH-II variants. To uncover the reasons for the low O$_2$ sensitivities of the ChCODH-II

variants, we solved the crystal structures of the variants A559W (Protein Data Bank (PDB) 7XDM), A559H (PDB 7XDN) and A559S (PDB 7XDP) (Fig. 3a and Supplementary Table 6). Given that the activity loss of most CODHs under aerobic conditions is closely related to the alteration or destruction of the active site C cluster, which is the most O_2-sensitive metal site[9,14,20], to maintain the structural integrity of the C cluster is vital to decrease O_2 sensitivity. Thus, we determined whether the structural integrity of the Fe–S clusters in the three variants was maintained and compared the anaerobic structure of A559W (PDB 7XDM) with the O_2-exposed structure of A559W (PDB 7ERR) prepared under aerobic conditions (Fig. 3a and Supplementary Fig. 6). When we examined the positions and the interacting residues around the B, C and D clusters of the variants, they were highly similar root mean squared deviation (r.m.s.d.) values: PDB 7XDM 0.296 Å, PDB 7ERR 0.333 Å, PDB 7XDN 0.325 Å and PDB 7XDP 0.291 Å for the 633 Cα atoms; PDB 7XDM 0.400 Å, PDB 7ERR 0.598 Å, PDB 7XDN 0.384 Å and PDB 7XDP 0.357 Å for all atoms to those of ChCODH-II WT (PDB 1SU7). Similarly, the r.m.s.d. between aerobic and anaerobic A559W structures (PDB 7ERR and 7XDM) was 0.174 Å (633 Cα atoms) and 0.432 Å (all atoms), as shown in Fig. 3a. Additionally, the omit maps (Fo–Fc (Fo, experimentally measured amplitude; Fc, model-based amplitude)) and Fe anomalous difference maps were similar to each other, which suggests that the Fe–S clusters of the variants have similar architectures to those of ChCODH-II WT and no loss of Fe and Ni (Supplementary Table 7 and Supplementary Figs. 6 and 7). However, the only local environments around the A559 mutation sites that affect the characteristics of the gas tunnel were significantly changed compared with those of ChCODH-II WT. In the A559W and A559H variants, the side chain of I580 was pushed away through the incorporation of the bulkier residue W559 or H559 instead of alanine, and the position of V582 was also slightly changed by making additional hydrogen bonds with W559 or H559. In the A559S variant, neither hydrogen bonding with V582 residues nor flipping of the I580 side chain was observed. Only the side chain of V582 moved towards S559 to form the additional van der Waals interaction.

The incorporation of W559, H559 or S559 made the gas tunnel in the variants narrower than that of ChCODH-II WT (Fig. 3b and Supplementary Fig. 4c). When we measured the radius of the gas tunnel at the bottleneck point of A559W using the CAVER program[21], it was reduced by approximately 1.02 Å compared with that of ChCODH-II WT (1SU7). Consequently, we deduced that the obstructed tunnels of the ChCODHs would not allow the transfer of both CO and O_2 to the active site, whereas other gas channels seem to be more selective for CO (Supplementary Fig. 8).

To estimate the structural rigidity of each tunnel of ChCODH-II WT and its variants, we calculated and compared the distances across the tunnel between two tunnel-forming residues (A/H/S/ W559 and F608) by molecular dynamics (MD) simulation (Fig. 3c,d and Supplementary Figs. 9 and 10). F608 as the opposite tunnel-forming residue with A/H/S/W559 was selected to more accurately reflect the local fluctuation of tunnels as the triad residues that form the bottleneck are not located precisely opposite to position 559. The distance and standard deviation (s.d.) values of A559W or A559S after 3 ns decreased to 10.486 Å and 0.395 Å or 10.467 Å and 0.630 Å, respectively, compared with those of the WT. The simulated distance of A559H and F608 increased to 13.730 Å, but the lower value (0.726 Å) of the local fluctuation was smaller than that in the WT. This analysis showed decreases in local fluctuation in the variant tunnels, which reflects that the constricted tunnels by point mutations become more rigid and more likely to limit O_2 accessibility compared with that of WT. In less O_2-sensitive Ni–Fe hydrogenases[22–25], there is evidence that constriction of the tunnels protects their active sites from O_2 attacks by serving as a barrier to the intrusion of molecular O_2. Therefore, these results suggest the

possibility that the mutation at position 559 is critical for the rigidity of the tunnel and affects O_2 access to the active site of ChCODH-II.

Efficient removal of industrial flue gas from a steel mill. Next, we assessed the activity of engineered A559W for different CO mixtures from synthetic and industrial flue gases (Fig. 4a, Supplementary Table 8 and Supplementary Fig. 11). Compared with the low-content CO (synthetic gas 1, 95% (v/v) CO and 5% (v/v) N_2), the relative activities of A559W were similarly observed as a deviation of up to 3.6% towards other CO mixtures: synthetic gases 1 (100%), 2 (95%) and (101%), blast-furnace gas (BFG, 91%), coke-oven gas (COG, 99%) and Linz–Donawitz converter gas (LDG) (96%). This indicates that ChCODH-II A559W has a consistent and sufficient selective performance for gaseous CO mixtures regardless of the low CO content and multicomponent mixtures, such as CO_2, CH_4 and H_2. In particular, the lack of severe inactivation by O_2 and unknown trace impurities in the industrial flue gases BFG, COG and LDG suggests that a less O_2-sensitive ChCODH variant can be used as a suitable and widely applicable biocatalyst for CO-containing flue gases from a variety of industrial environments.

Finally, to evaluate the performance of the low-O_2-sensitive ChCODH-II variant for the removal of gaseous CO, we tested the variants as an oxidizing biocatalyst in 50% (v/v) CO-saturated 0.2 M N-(2-hydroxyethyl)piperazine-N′-(2-ethanesulfonic acid) (HEPES, pH 8) with or without dissolved 170 μM O_2 (~13.4%, v/v). Figure 4b indicates that ChCODH-II WT and A559W readily consumed CO within 2.5 hours under anaerobic conditions, whereas under O_2, only A559W consumed CO within 3 hours. This experiment confirmed that A559W, unlike ChCODH-II WT, can sufficiently and selectively consume CO without severe O_2 inactivation. Under the aerobic conditions, A559W seemed to traverse a lag phase in half-an-hour, probably until the enzyme reactivation by CO could overcome O_2-induced arrest. Ni–Fe CODHs can be recovered when CO or dithionite is added[26]. A plausible explanation is that CO can serve as a weak reductant for A559W recovery in the manner of dithionite-treated ChCODH-II[9,14,26]. Furthermore, we observed the reversibility of the inactivation of A559W after a short-term exposure to air (Supplementary Fig. 12). ChCODH-II WT is almost irreversibly inactivated by O_2. In contrast, the activity of the variant A559W towards CO reversibly and rapidly recovers from the inactive state caused by air exposure. This reversibility of the O_2 inhibition could be very interesting for industrial applications. However, the exact mechanism of this remarkable reversibility is currently unclear and needs to be further explored. Finally, for practical application purposes, we monitored the CO utilization of A559W using real LDG flue gas from a steel mill in the presence of dissolved O_2 (~13.4%, v/v). The variant A559W displayed an impressive capability to remove the total amount of CO (53.4%) from LDG (Fig. 4c,d), but no CO consumption was observed for ChCODH-II WT. Even under atmospheric conditions of approximately 250 μM O_2 (~20%, v/v), CO uptake of 33% was observed for A559W (Supplementary Fig. 13). Moreover, we compared the CO consumptions of variants A559H, A559S and A559W using 50% (v/v) CO-saturated buffer and LDG-saturated buffer (Supplementary Fig. 14). A559W had the fastest CO removal rate in the presence of dissolved O_2 (~13.4%, v/v). This may be because the catalytic efficiency of A559H and A559S is lower than that of A559W, as shown in Table 1. We considered A559W to be the most efficient biocatalyst for the removal of CO. Thus, the less O_2-sensitive biocatalyst A559W was shown to enable the enhanced CO bioconversion under near-atmospheric conditions and demonstrated outstanding performance in complete CO removal from steel-mill flue gas (LDG).

In addition to an efficient CO consumption, A559W must have the sustainable capacity to be reused and recycled for the treatment of industrial flue LDG. Immobilized biocatalysts can be employed as a simple reuse and recovery method for cost savings in industrial
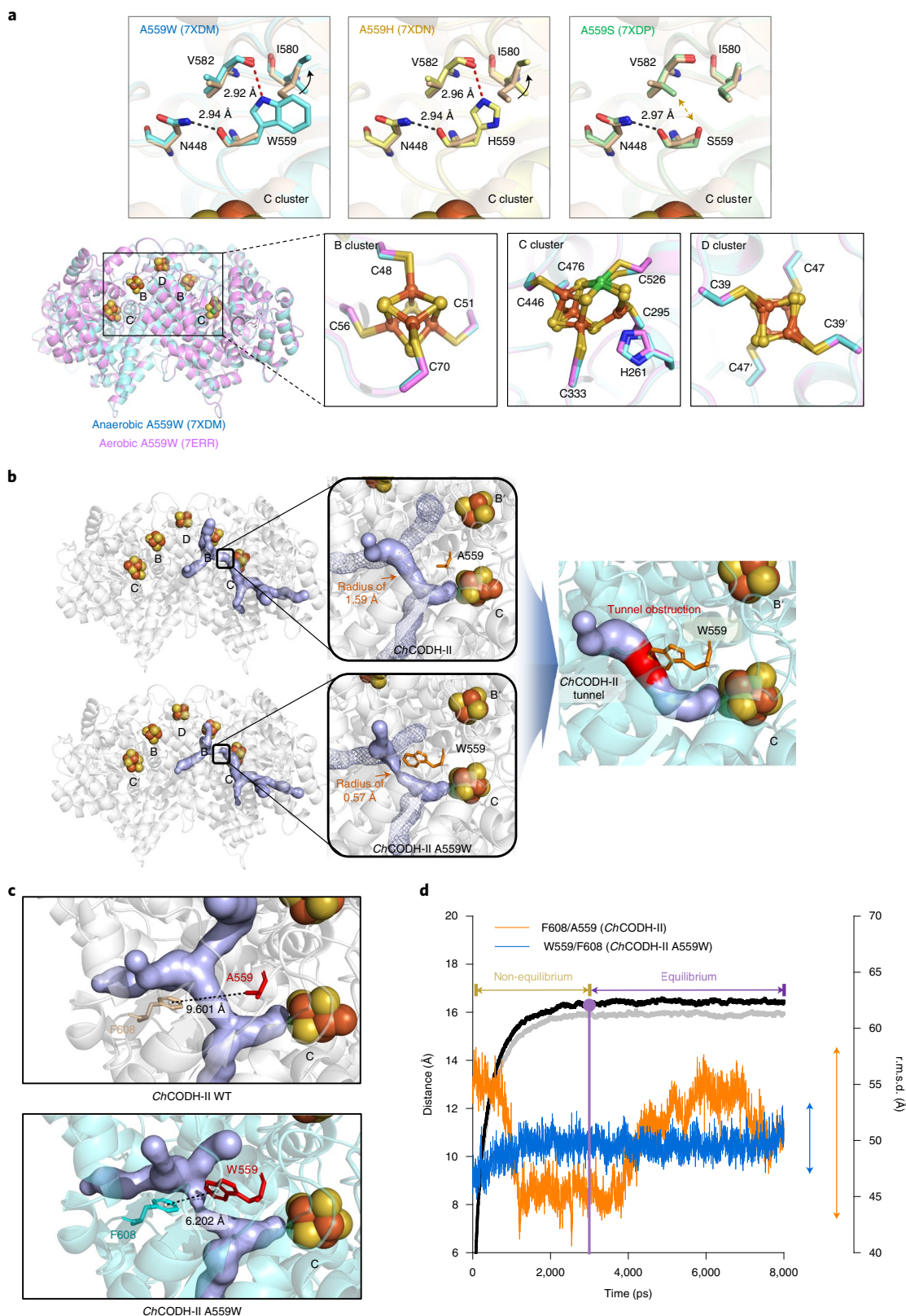
Fig. 3 | Structures of less O$_2$-sensitive *Ch*CODH-II variants. a, Bottleneck residues of *Ch*CODH-II variants and metal clusters of A559W. Structures of *Ch*CODH-II WT and the A559 variants are superimposed (top row). Dotted lines and arrows denote hydrogen bonds and van der Waals interactions, respectively. The clusters of aerobic and anaerobic A559W are superimposed (bottom row). Fe, orange; S, yellow; Ni, green. **b**, Superimposition of *Ch*CODH-II WT and A559W (highlighted in red). **c**, Distances between tunnel-forming residues A559/W559 and F608. **d**, Distance fluctuations between F608 and A/W559 in the MD simulation. Each local fluctuation (*y* axis) in the WT (orange) and A559W (blue) was calculated. Values of the r.m.s.d of Cα atoms of WT (grey) and A559W (black) calculated during 8 ns are shown on the right. The vertical arrows indicate the maximum and minimum distances in WT (orange) and A559W (blue) after the equilibrium state at 3 ns (violet vertical line; see Supplementary Fig. 9).
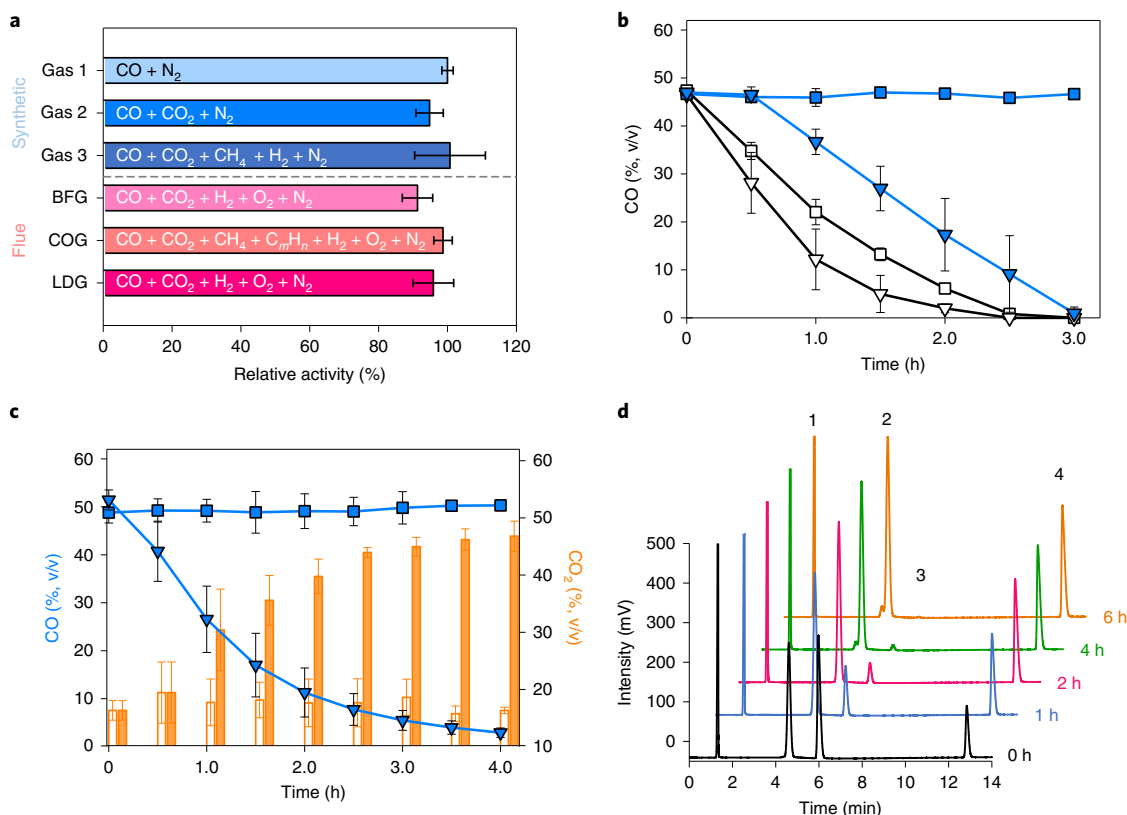
Fig. 4 | Efficient CO removal of *Ch*CODH-II A559W. a, Influence of gas mixtures on *Ch*CODH-II A559W. Synthetic mixtures and industrial flue gases were used for the testing, and the relative activities of A559W were determined by comparison with the enzyme activity (100%) for synthetic gas 1. See Methods for detailed gas compositions. Constituents of each gas mixture are displayed within bars. The data represent the mean ± s.d., as determined from $n=3$ independent experiments. **b**, CO removal by *Ch*CODH-II A559W with different O_2 content. In the absence (open symbols) of O_2, gaseous CO/N_2 (50:50, v/v) was consumed by either *Ch*CODH-II (squares) or the A559W variant (reverse triangles). Conversely, in the presence (closed symbols) of O_2 (170 μM O_2 (~13.4%, v/v)), only A559W utilized CO as a substrate. The data represent the mean ± s.d., as determined from $n=3$ independent experiments. **c**, CO conversion of *Ch*CODH-II A559W using LDG with O_2. Experiments on the CO removal of waste LDG from Hyundai's steel mill were carried out in a similar manner for *Ch*CODH-II WT (squares) and A559W (reverse triangles) under near-atmospheric conditions (170 μM O_2 (~13.4%, v/v)). The CO_2 produced in the reaction of either *Ch*CODH-II (white bars) or A559W (orange bars) was monitored. The data represent the mean ± s.d., as determined from $n=3$ independent experiments. **d**, Gas chromatography (GC) analysis of the reaction products from LDG gas and A559W. The GC chromatograms were obtained after the reaction of A559W using LDG flue gas. The products were identified by comparison with authentic standards (peak 1, H_2; peak 2, N_2; peak 3, CO; peak 4, CO_2).

applications. Figure 5 shows that the conversion rate of CO by immobilized A559W is maintained through repeated cycles of reuse and in the presence of O_2. The immobilized A559W was incubated at room temperature (r.t.) using flue LDG for the first ten cycles (Fig. 5a,b), and LDG with dissolved 170 μM O_2 (~13.4%, v/v) was then used for the second ten cycles (Fig. 5a,c). In the absence of O_2, there was no loss of conversion rate during ten cycles, which indicates that the enzyme is still active after repeated uses and is not inhibited by the product CO_2 or other gas impurities from LDG. In the presence of O_2, ten cycles of the reaction also exhibited complete oxidation of CO to give CO_2, which indicates that the immobilized A559W is unaffected by O_2 interference. The results suggested that this engineered variant can efficiently remove CO from steel-mill flue gases that contain varying levels of CO and O_2, even after repeated reuse, and might be adaptable for future industrial applications.

Conclusions

Resistance to atmospheric O_2 exposure is a rare feature among enzymes that express CO dehydrogenase activity. To date, the only known aerobic CODH is the Mo-Cu CODH enzyme. In contrast, Ni-Fe CODHs are highly sensitive to O_2, with the exception of two

slow CODHs, *Ch*CODH-IV and *Dv*CODH, which are less sensitive to O_2. Thus, the use of low-O_2-sensitive *Ch*CODH biocatalysts with a marked increase in rate efficiency would provide the advantage of an efficient CO conversion for various waste gases and syngases that contain O_2 (for example, biomass and plastics) in industry or applied green chemistry. Based on our analyses and a rational approach, we selected different strategic points in the enzyme to generate variants able to maintain the high activity rates of *Ch*CODH-II combined with the low O_2 sensitivity of *Ch*CODH-IV. This study thus points towards an effective avoidance of the rapid O_2 inactivation of Ni-Fe CODHs through an increased selectivity of the gas tunnel. Catalytic activity and decreased O_2 sensitivity are often considered to be trade-offs, but the *Ch*CODH-II variants show how to overcome such limits.

In summary, our study presents the key discoveries that one position is enough to decrease the sensitivity to O_2 and that the second, unaffected tunnel seems to be highly specific for CO/CO_2 rather than O_2; it provides some reasons as to why all anaerobes have such highly O_2-sensitive CODHs even though one point mutation would be enough to drastically improve their CODHs by conferring a faster turnover and decreased O_2 sensitivity but probably less efficient in vivo under a lower CO environment and it suggests that the
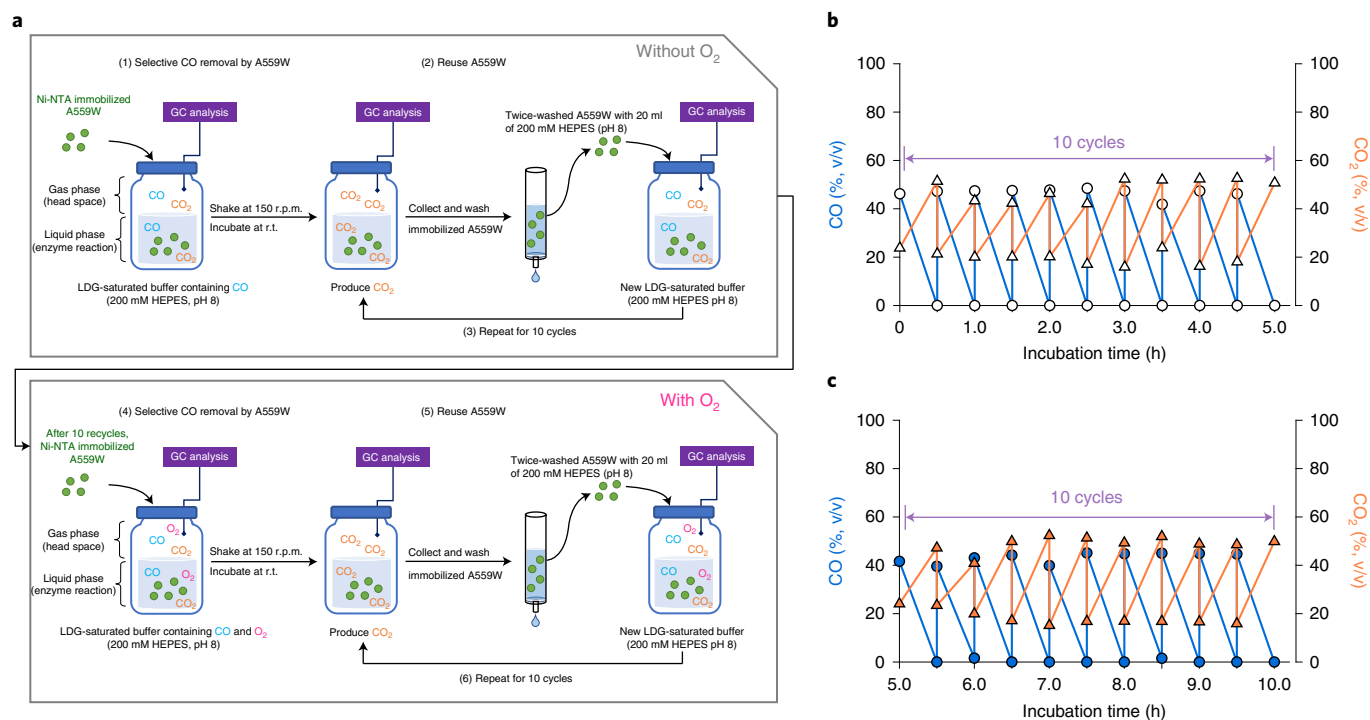
Fig. 5 | Repeated reuse of immobilized A559W. a, A schematic for the experimental procedure. The reaction was performed at r.t. using a rubber-sealed serum bottle (115 ml) with 20 ml of head space (CO of 446 μmol) and 95 ml of reaction buffer (see Methods for details). **b**, Reusability of immobilized *Ch*CODH-II A559W using LDG. The removal of CO (circles) from flue LDG by *Ch*CODH-II A559W without O_2 (open symbols) was equivalent to the CO_2 production (triangles). The enzyme with a His_6-tag was immobilized on a Ni-NTA resin for 20 cycles of reuse with no severe losses in the conversion rate. The first ten cycles of reaction were initiated in the absence of O_2 by the addition of the immobilized A559W enzyme (500 U mg^{-1} immobilized protein). The immobilized enzyme was recovered through a disposable open column, washed twice with 200 mM HEPES/NaOH buffer pH 8 and reused after each reaction. **c**, Reusability of immobilized *Ch*CODH-II A559W using LDG with O_2 (closed symbols). After the first ten cycles using LDG, the second ten cycles were then performed in the presence of 170 μM O_2 (~13.4%, v/v).

next step in applying these designed biocatalysts will be coupling on an electrode or direct transfer of the reducing power to another system (for example, CO_2 fixation into formate). Alternatively, these variants could be implanted in anaerobic bacteria to increase their performance as bioconverters. This work provides concrete proof that CODHs can be tailored for industrial or gas-cleaning processes by engineering the selectivity of their gas tunnels.

Methods

Gene synthesis and cloning. The genes encoding *Ch*CODH-II (CHY_0085), *Ch*CODH-IV (CHY_0736) and *Dv*CODH (DVU_2098) with *Nde*I and *Bam*HI restriction sites were optimized, synthesized and sequence verified by Macrogen based on their GenBank sequences (accession nos. NC_007503 and NC_002937). The resulting fragments were cloned into pET28a (Novagen) that contained a His tag and an additional thrombin-cutting site. Site-directed variants were constructed using the QuikChange site-directed mutagenesis method from Stratagene through *Pfu* DNA polymerase. PCR products were incubated for 60 min at 37 °C with *Dpn*I (2 U μl^{-1}) to remove the parental plasmid. The *Dpn*I-treated plasmid was purified and transformed into the *E. coli* DH5α strain. Point mutations were verified by DNA sequencing. The resulting pET28a-*Ch*CODH-II, pET28a-*Ch*CODH-IV, pET28a-*Dv*CODH and all of the variant plasmids were transformed into *E. coli*-BL21 that harboured pRKISC[27].

Protein expression and purification. Cultures were grown in a modified TB medium supplemented with 0.02 mM $NiCl_2$, 0.1 mM $FeSO_4$, 2 mM L-cysteine, kanamycin (50 μg ml^{-1}) and tetracycline (10 μg ml^{-1}) at 37 °C. When the culture reached an OD_{600} of 0.4–0.6, the expression of recombinant CODHs and its variants was induced by the addition of 0.2 mM IPTG (isopropyl β-D-1-thiogalactopyranoside) supplemented with 0.5 mM $NiCl_2$, 1 mM $FeSO_4$ and 50 mM KNO_3 at 30 °C after N_2 fluxing. After overnight induction at 30 °C, the cells were harvested and stored aerobically at −70 °C. All the purification steps were conducted in an anoxic glove box (model B, COY Laboratory Products) under

an atmosphere of 95% (v/v) N_2/5% H_2 (v/v) at r.t. Sonication was carried out anaerobically on ice.

Cell lysates were centrifuged and purified by Ni-NTA affinity chromatography (Qiagen) with a standard buffer that contained 2 mM DTE and 2 μM resazurin, but DTE and resazurin were omitted from the washing and elution steps during the O_2 inactivation assay. Protein concentrations were determined using the Bradford method. When the purified proteins were subjected to SDS-PAGE on 12% gels, all the variants were detected as a single soluble band whose size (69 kDa) approximately corresponded to the calculated size of the proteins (67 kDa) with the His_6-tag (2 kDa). Western blot analyses using anti-His-tag antibodies were also carried out to confirm the presence of the His tag and putative degradation of the His-tagged protein. For the crystallization of *Ch*CODH-II variants (A559W, A559H and A559S) under anaerobic conditions, further purification was anaerobically performed in an anoxic glove box (model B, COY Laboratory Products Inc.) by size-exclusion chromatography (HiLoad 16/600 Superdex 200 prep grade, GE Healthcare Bio-Sciences), which was previously equilibrated with a buffer that contained 20 mM Tris-HCl pH 7.5 and 3 mM DTT. For crystallization of the aerobic A559W variant, the protein purification step using Ni-NTA resin was conducted in a similar manner to that above but under aerobic conditions (outside the anaerobic chamber). Further purification by size-exclusion chromatography was also performed aerobically with a buffer that contained 20 mM Tris-HCl pH 7.5 and 3 mM DTT.

Size-exclusion chromatography with multiangle light scattering. Size-exclusion chromatography with multiangle light scattering experiments on the *Ch*CODH-II A559W variant were performed aerobically using a fast protein liquid chromatography (FPLC) system (GE Healthcare) connected to a Wyatt MiniDAWN TREOS MALS instrument and a Wyatt Optilab rEX differential refractometer. A Superdex 200 10/300 GL (GE Healthcare) gel-filtration column was pre-equilibrated with a buffer that contained 20 mM Tris-HCl pH 7.5 and 3 mM DTT and normalized using ovalbumin protein from hen egg white (Sigma–Aldrich). Proteins were injected (1 mg), and elution was performed at a flow rate of 0.4 ml min^{-1}. Data were analysed using the Zimm model for static light-scattering data fitting and graphed using an EASI graph with an ultraviolet peak in ASTRA V software (Wyatt), as shown in Supplementary Fig. 15.

Activity measurement. CO oxidation activity was measured at 30 °C after saturation with CO using screw-cap cuvettes with a CO head space. The activity was assayed by observing the CO-dependent reduction of oxidized EV (EV$_{ox}$, ε_{578} = 10,000 M^{-1} cm^{-1}) (ref. [28]). The reactions were started by enzyme injection (0.1–0.2 µg) into a screw-cap cuvette that contained 2 ml of reaction buffer (20 mM EV$_{ox}$, 0–250 µM O$_2$, 50 mM HEPES/NaOH buffer pH 8 with saturated CO from 50 ml of stock solution flushed with CO gas for 1 h) (ref. [29]). When the activity of the enzyme is measured, trace O$_2$ during the enzyme preparation may slightly affect the CODH activity due to the lack of a reducing agent (DTE). Thus, small differences can occur in the measurement of the specific activity. For practical applications, the enzymatic oxidation of CO as a carbon and energy source at this mild temperature has the advantages of a spontaneous reaction without the need for additional energy and of easy coupling with other mesophilic enzymes, such as formate dehydrogenase.

To test the effect of O$_2$ inactivation, we measured the residual activity of the enzyme at appropriate O$_2$ concentrations. Before assaying the residual activity, the CODHs (2–4 µg) were incubated in 50 mM HEPES (final volume of 200 µl) for 2 min with O$_2$ addition, and then the reaction mixture was diluted 200–400 times to give a final O$_2$ concentration below 0.6 µM. One unit of CODH activity was defined as the amount of enzyme required to reduce 1 µmol of EV$_{ox}$ per min at 30 °C and pH 8.

Kinetic analysis. For calculations of the kinetic parameters for EV$_{ox}$, a CO-saturated buffer that corresponded to 0.91 mM CO (99.998% according to Henry's law) was used at 30 °C. The headspace of a rubber-septum-stopped cuvette that contained 0.5–8 mM EV in 50 mM HEPES/NaOH buffer (pH 8) was purged with CO for 1 h. To monitor the initial velocity of the CODHs, the reaction was initiated by an injection of recombinant CODHs (0.1–0.2 µg). For measurement of the kinetic parameters towards CO, two CO-saturated buffers that corresponded to 0.91 mM CO (99.998% according to Henry's law) and 45.5 µM CO (5% CO (v/v)/95% N$_2$ (v/v) according to Henry's law) were used at 30 °C. Three CO concentrations (10 µM, 20 µM and 40 µM) and two CO concentrations (80 µM and 160 µM) that each contained a final concentration of 20 mM EV in 50 mM HEPES pH 8 buffer were immediately prepared before the reaction by diluting two CO-purged buffers of 0.0455 mM and 0.91 mM, respectively. The enzyme reaction was initiated by injecting each reaction buffer with different CO concentrations (0.01–0.16 mM) into the enzyme (0.1–0.2 µg). The absorbance change at 578 nm was spectrophotometrically monitored at 30 °C in an anoxic glove box. The kinetic parameters ($k_{cat,app}$ and $K_{M,app}$) for CO and EV$_{ox}$ were calculated by the Hanes–Woolf equation (Supplementary Fig. 16). All of the enzymatic activities were determined in triplicate. For K_I determinations, IC$_{50}$ values (Supplementary Fig. 17) were calculated using nonlinear regression (four-parameter logistic curve). [S] is the concentration of the substrate CO. Subsequent K_I values were calculated using equation (1) (ref. [30]):

$$K_I = IC_{50}/(1 + [S]/K_M) \qquad (1)$$

Crystallization and structural determination. To solve the crystal structures of the *Ch*CODH-II A559W, A559H and A559S variants under anaerobic conditions, crystals were grown using the hanging drop method by mixing 2 µl of protein (10 mg ml^{-1}) with 2 µl of reservoir solution, which consisted of 0.1 M HEPES/NaOH pH 7.5, 200 mM MgCl$_2$ and 25% (w/v) polyethylene glycol 3350. The crystals were transferred to a solution that contained the reservoir solution with 7.5% (w/v) glycerol for cryoprotection. Data were collected at 100 K in 1° oscillation at the 11C and 5C beamlines of the Pohang Light Source with wavelengths of 0.9794 and 1.0000 Å, respectively. The crystals were diffracted to resolutions of 1.74 Å, 1.80 Å and 1.84 Å, and the diffraction data were processed and scaled using the HKL2000 software package[31]. The structures were solved by the molecular replacement method using the *Ch*CODH-II WT model (PDB 1SU7) as a probe[32]. Subsequent manual model building was performed using the Coot program[33], and restrained refinement was carried out using PHENIX (version 1.19.2_4158)[34] and CCP4 refmac5[35] in the absence of hydrogen atoms. Several rounds of model building, simulated annealing, positional refinement and individual B-factor refinement were performed using Coot and PHENIX. Ramachandran statistics (%) of favoured, allowed and outliers were as follows: 97.0, 2.7 and 0.3 for A559W, 96.2, 3.6 and 0.2 for A559H and 96.4, 3.3 and 0.3 for A559S. Supplementary Table 6 lists the refinement statistics. The atomic coordinates and structural factors were deposited in the Protein Data Bank (PDB 7XDM, 7XDN and 7XDP).

Crystals of the *Ch*CODH-II A559W variant were grown under aerobic conditions using the sitting drop method by mixing 0.2 µl of protein (10 mg ml^{-1}) with 0.2 µl of reservoir solution that consisted of 0.1 M HEPES/NaOH pH 7.0, 50 mM MgCl$_2$ and 25% (w/v) polyethylene glycol 3350. The crystals were transferred to a solution that contained the reservoir solution and 5% (w/v) glycerol for cryoprotection. Data were collected at 100 K in 1° oscillation at the 5C beamlines of the Pohang Light Source with a wavelength of 1.0000 Å. The structure calculation methods were identical to those used for the anaerobic proteins. Ramachandran statistics (%) of favoured, allowed and outliers were 96.7, 3.2 and 0.2, respectively. The atomic coordinates and structure factors were deposited in the Protein Data Bank (PDB 7ERR).

X-ray absorption spectroscopy and Fe anomalous difference map. Fluorescence scans were performed on crystals of anaerobic *Ch*CODH-II A559W, A559H and A559S variants at the 11C and 5C beamlines of the Pohang Light Source near the X-ray absorption edge of Fe ions. The anomalous diffraction data were collected at the peak position of the Fe absorption edge (7.135 keV). Anomalous datasets were processed and scaled using the HKL2000 software package[31]. Supplementary Table 7 lists the anomalous data-collection statistics. An anomalous difference Fourier map calculation was performed using the fast Fourier transform in the CCP4 refmac5 program[35].

Molecular dynamics simulation of *Ch*CODHs. The complex structure was optimized by MD simulation using Discovery Studio software (BIOVIA) with the CHARMm force field[36]. The structures of WT (PDB 1SU7), A559W (aerobic, PDB 7ERR; anaerobic, PDB 7XDM), A559H (PDB 7XDN) and A559S (PDB 7XDP) were analysed for simulation. The protein force field parameters were taken from the CHARMm force field. The protonation states of the acidic and basic residues in the protein were analysed using the calculated protein ionization and residue pK protocol. Protons were added to the input CODH structure based on the ionization states of the titratable groups obtained from the Discovery Studio protocol, which calculates the ionization state of a protein at a specified pH (8.0). The transferable intermolecular potential with 3 points (TIP3P) water model[37] was used for the solvent. For the Fe–S clusters, we used the force-field parameters provided by Discovery Studio (Supplementary Table 9). The C clusters of the protein were fixed to prevent an unnatural conformation. Solvation was used to simulate the more natural behaviour of tunnels that consisted of amino acids, which are affected by solvent molecules such as surface residues. The protein was solvated with 19,873 water molecules and 53 sodium and 54 chlorine ions for the WT, 20,924 water molecules and 66 sodium and 55 chlorine ions for the A559W mutant, 19,418 water molecules and 60 sodium and 51 chlorine ions for the A559H mutant and 20,045 water molecules and 60 sodium and 53 chlorine ions for the A559S mutant to create a 0.145 M NaCl solution in a cubic unit cell, thereby neutralizing the protein charge. The periodic boundary condition was set to prevent truncation effects. The particle mesh Ewald method was used to calculate long-range electrostatic forces[38]. All the bonds with hydrogen were constrained with the SHAKE algorithm[39]. A standard dynamics cascade protocol was performed to apply nanoscale MD simulation in Discovery Studio. This protocol consisted of five steps. For minimization, the steepest descent algorithm with a max step of 1,000 and a r.m.s. gradient of 1.0 was used first. For a more detailed minimization, the Adopted Basis Newton–Raphson algorithm with a max step of 2,000 and an r.m.s. gradient of 0.1 were applied. After a brief minimization process, the system was heated for 4 ps in the isothermal–isobaric (NPT) ensemble to a temperature of T = 300 K from T = 50 K and a pressure of P = 1 atm. Next, the system was equilibrated for 10 ps in the NPT ensemble at a temperature of T = 300 K and a pressure of P = 1 atm. A subsequent production run of 10 ps followed by a production run of 10 ps were carried out in the NPT ensemble. The full system of MD was run for 8 ns with the NPT conditions. The trajectories were saved every 2 ps for analysis. Whether the protein reached an equilibrated state was evaluated by the energy and volume under the NPT ensemble[40].

Gas chromatography analyses. The amounts of CO and CO$_2$ in the head phase were measured using an Agilent 7890B gas chromatograph equipped with a thermal conductivity detector (GC-TCD) and a carbon molecular sieve column (Carboxen 1000 with a 60/80 mesh, Supelco). During the GC-TCD analysis, the initial oven temperature was 35 °C for 5 min, which was gradually increased to 225 °C at a rate of 20 °C min^{-1}. The injector and detector temperatures were 250 and 225 °C, respectively, and the flow rate of the carrier gas (Ar) was maintained at a constant rate of 30 ml min^{-1}. A rubber-sealed serum bottle (115 ml) that contained 20 ml of head space (CO of 446 µmol) and 95 ml of reaction buffer (20 mM EV$_{ox}$, 0–200 mM O$_2$, 200 mM HEPES/NaOH buffer pH 8 with purged CO/N$_2$ (50:50, v/v)) or LDG gas for 1 h was used for the reactions, which were started by enzyme injection (50 U) at r.t. and 150 revolutions per minute (rpm) shaking. For the enzyme reusability of A559W, each cycle of reaction was initiated at r.t. and pH 8 by the addition of the immobilized variant A559W enzyme (500 U mg^{-1} immobilized protein) into LDG-purged buffer with 40 mM EV$_{ox}$ (see the next section for details). The flue gases BFG (CO, 25.45% (v/v); CO$_2$, 23.56% (v/v); H$_2$, 3.75% (v/v); O$_2$, 0.01% (v/v); N$_2$, 46.71% (v/v)), COG (CO, 6.15% (v/v); CO$_2$, 2.42% (v/v); CH$_4$, 24.16% (v/v); C$_m$H$_n$, 3.07% (v/v); H$_2$, 55.4% (v/v); O$_2$, 0.1% (v/v); N$_2$, 8.63% (v/v)) and LDG (CO, 53.17% (v/v); CO$_2$, 18.51% (v/v); H$_2$, 1.43% (v/v); O$_2$, 0.11% (v/v); N$_2$, 26.77% (v/v); unknown, 0.1% (v/v)) were acquired from Hyundai Steel.

Reusability of immobilized A559W. The soluble protein from the cell lysate (15–25 ml of lysis buffer per gram of wet cell weight) for immobilization was incubated with Ni-NTA agarose (as an immobilization carrier) with shaking at 80–100 rpm for at least 2 h in an anaerobic chamber. After 2 h of incubation, when the soluble proteins, which were brownish due to the Fe–S clusters, were sufficiently bound to the bluish Ni-NTA agarose, the resin colour visibly changed to dark brown. The resultant Ni-NTA immobilized proteins were washed with 1 column volume (20 ml disposable gravity flow column) of wash buffer (20 mM imidazole, 300 mM NaCl, 50 mM sodium phosphate, pH 8) to eliminate unbound

proteins. A small aliquot of these immobilized proteins was eluted to check the specific activity of the protein in the same manner described in the protein purification section above. In addition, we measured the apparent units of protein per immobilization bead volume owing to the difficulty of determining the exact amounts of immobilized proteins.

The reaction buffer for the enzyme reaction was anaerobically prepared in a rubber-capped serum bottle (115 ml) with 95 ml of buffer solution (40 mM EV_{ox}, 200 mM HEPES, pH 8), transferred from the anaerobic chamber, and then purged with LDG for 1 h. The headspace gas of the purged serum bottle was further analysed by the GC-TCD method above. The main enzyme reactions were performed for 20 consecutive cycles: 10 cycles using LDG only and another 10 cycles using LDG with dissolved O_2. For the 10 cycles without O_2, the first reaction cycle was performed at r.t. and 150 rpm with shaking by syringe injection of the immobilized protein (50 U mg^{-1} immobilized protein) into the LDG-purged serum bottle. After 30 min of incubation on the shaker with the bottle placed horizontally, the gas sample from the headspace in the reaction bottle was analysed by a GC instrument. Next, the immobilization beads used after the reaction were collected in a disposable column, and the collected immobilized proteins were washed twice with 20 ml of wash buffer (200 mM HEPES, pH 8). This recycled protein was consecutively reused in the next cycle with a freshly prepared LDG-purged reaction buffer. In the same manner, the immobilized enzyme reactions were repeated for ten cycles.

For the ten cycles using LDG with dissolved O_2, we also prepared the O_2-purged buffer, in which the reaction buffer (200 mM HEPES, pH 8) was purged with O_2 (100%, v/v) for 1 h. The rubber-capped serum bottle (115 ml) with 82.3 ml of reaction buffer (40 mM EV_{ox} for a 95 ml final volume, 200 mM HEPES, pH 8) was transferred from the anaerobic chamber and then purged with LDG for 1 h. Then, 12.7 ml of the O_2-purged buffer was injected into the LDG-purged reaction buffer (final O_2 concentration of 170 μM). The gas sample from the headspace in the reaction buffer was analysed by GC. As in the previous experiments using only LDG-purged buffer, the enzyme reactions using LDG with dissolved O_2 were repeatedly performed by incubation of the same immobilized protein after ten cycles of reuse. All the gas samples from the ten reaction cycles in the presence of LDG and O_2 were analysed by GC.

Bioinformatics analysis. Searches for amino acid sequence homologues and multiple sequence alignments were performed using BLAST and ClustalW, respectively. The hybrid-cluster proteins with no CODH activity were excluded from the sequence analysis. Conserved domains and clusters of orthologous groups of proteins were analysed using the CD-Search tool at the National Center for Biotechnology Information (http://www.ncbi.nlm.nih.gov). Structural alignments for the assessment of the topological similarity of protein structures were analysed using TM score software[41] (https://zhanggroup.org/TM-align). Phylogenetic trees were constructed using MEGA 10 software[42] with the neighbour-joining method (1,000 replicates). Bootstrap values (>90%) are displayed at the branch points. Non-redundant reference sequences (1,710 proteins) of Ni–Fe CODHs belonging to id_1151 (the number in clusters of orthologous groups) from eggNOG 5.0[43] (orthologues database) were manually checked for completeness and length. Sequences shorter than 620 amino acids and longer than 700 amino acids were not used for alignment, and sequences longer than 650 amino acids were shortened. The resultant 208 amino acid sequences were used in the phylogenetic analysis. The optimal tree with the sum of branch length = 33.96697452 is shown. All the ambiguous positions were removed for each sequence pair (pairwise deletion option). There were a total of 854 positions in the final dataset. Moreover, the substrate tunnel analyses were carried out using the tool of CAVER3.0 software[21] (http://www.caver.cz).

Reporting summary. Further information on research design is available in the Nature Research Reporting Summary linked to this article.

Data availability

The datasets generated during and/or analysed during the current study are available from the corresponding authors upon reasonable request. MD trajectories of a total of 5 ns are available on Zenodo at https://doi.org/10.5281/zenodo.6865415. The atomic coordinates and structure factors for the *Ch*CODH-II A559 variants have been deposited in the Protein Data Bank under accession codes PDB 7ERR, 7XDM, 7XDN and 7XDP.

References

1. Ragsdale, S. W. Life with carbon monoxide. *Crit. Rev. Biochem. Mol. Biol.* **39**, 165–195 (2004).
2. Choi, E. S., Min, K., Kim, G. J., Kwon, I. & Kim, Y. H. Expression and characterization of *Pantoea* CO dehydrogenase to utilize CO-containing industrial waste gas for expanding the versatility of CO dehydrogenase. *Sci. Rep.* **7**, 44323 (2017).
3. Hwang, H. W. et al. Two-stage bioconversion of carbon monoxide to biopolymers via formate as an intermediate. *Chem. Eng. J.* **389**, 124394 (2020).
4. Kim, T. W. et al. A biological process effective for the conversion of CO-containing industrial waste gas to acetate. *Bioresour. Technol.* **211**, 792–796 (2016).
5. Liew, F. et al. Gas fermentation—a flexible platform for commercial scale production of low-carbon-fuels and chemicals from waste and renewable feedstocks. *Front. Microbiol.* **7**, 694 (2016).
6. Anderson, M. E., Derose, V. J., Hoffman, B. M. & Lindahl, P. A. Identification of a cyanide binding-site in CO dehydrogenase from *Clostridium thermoaceticum* using EPR and ENDOR spectroscopies. *J. Am. Chem. Soc.* **115**, 12204–12205 (1993).
7. Shima, S. & Ataka, K. Isocyanides inhibit [Fe]-hydrogenase with very high affinity. *FEBS Lett.* **585**, 353–356 (2011).
8. Ragsdale, S. W., Ljungdahl, L. G. & Dervartanian, D. V. Isolation of carbon monoxide dehydrogenase from *Acetobacterium woodii* and comparison of its properties with those of the *Clostridium thermoaceticum* enzyme. *J. Bacteriol.* **155**, 1224–1237 (1983).
9. Domnik, L. et al. CODH-IV: a high-efficiency CO-scavenging CO dehydrogenase with resistance to O_2. *Angew. Chem. Int. Ed.* **56**, 15466–15469 (2017).
10. Jeoung, J. H., Martins, B. M. & Dobbek, H. X-ray crystallography of carbon monoxide dehydrogenases. *Methods Mol. Biol.* **1876**, 167–178 (2019).
11. Rovaletti, A., Bruschi, M., Moro, G., Cosentino, U. & Greco, C. The challenging in silico description of carbon monoxide oxidation as catalyzed by molybdenum–copper CO dehydrogenase. *Front. Chem.* **6**, 630 (2019).
12. Zhang, B., Hemann, C. F. & Hille, R. Kinetic and spectroscopic studies of the molybdenum–copper CO dehydrogenase from *Oligotropha carboxidovorans*. *J. Biol. Chem.* **285**, 12571–12578 (2010).
13. Svetlitchnyi, V., Peschel, C., Acker, G. & Meyer, O. Two membrane-associated NiFeS–carbon monoxide dehydrogenases from the anaerobic carbon-monoxide-utilizing eubacterium *Carboxydothermus hydrogenoformans*. *J. Bacteriol.* **183**, 5134–5144 (2001).
14. Merrouch, M. et al. O_2 inhibition of Ni-containing CO dehydrogenase is partly reversible. *Chemistry* **21**, 18934–18938 (2015).
15. Wu, M. et al. Life in hot carbon monoxide: the complete genome sequence of *Carboxydothermus hydrogenoformans* Z-2901. *PLoS Genet.* **1**, 563–574 (2005).
16. Liebgott, P. P. et al. Relating diffusion along the substrate tunnel and oxygen sensitivity in hydrogenase. *Nat. Chem. Biol.* **6**, 63–70 (2010).
17. Seravalli, J. & Ragsdale, S. W. ^{13}C NMR characterization of an exchange reaction between CO and CO_2 catalyzed by carbon monoxide dehydrogenase. *Biochemistry* **47**, 6770–6781 (2008).
18. Zhu, G. H. & Spreitzer, R. J. Directed mutagenesis of chloroplast ribulose-1,5-bisphosphate carboxylase/oxygenase: loop 6 substitutions complement for structural stability but decrease catalytic efficiency. *J. Biol. Chem.* **271**, 18494–18498 (1996).
19. Bonam, D., Murrell, S. A. & Ludden, P. W. Carbon monoxide dehydrogenase from *Rhodospirillum rubrum*. *J. Bacteriol.* **159**, 693–699 (1984).
20. Drake, H. L. Occurrence of nickel in carbon monoxide dehydrogenase from *Clostridium pasteurianum* and *Clostridium thermoaceticum*. *J. Bacteriol.* **149**, 561–566 (1982).
21. Chovancova, E. et al. CAVER 3.0: a tool for the analysis of transport pathways in dynamic protein structures. *PLoS Comput. Biol.* **8**, e1002708 (2012).
22. DeMirci, H. et al. Structural adaptation of oxygen tolerance in 4-hydroxybutyrl-CoA dehydratase, a key enzyme of archaeal carbon fixation. Preprint at *bioRxiv* https://doi.org/10.1101/2020.02.05.935528 (2020).
23. Fritsch, J. et al. The crystal structure of an oxygen-tolerant hydrogenase uncovers a novel iron-sulphur centre. *Nature* **479**, 249–252 (2011).
24. Montet, Y. et al. Gas access to the active site of Ni–Fe hydrogenases probed by X-ray crystallography and molecular dynamics. *Nat. Struct. Biol.* **4**, 523–526 (1997).
25. Kalms, J. et al. Krypton derivatization of an O_2-tolerant membrane-bound [NiFe] hydrogenase reveals a hydrophobic tunnel network for gas transport. *Angew. Chem. Int. Ed.* **55**, 5586–5590 (2016).
26. Feng, J. & Lindahl, P. A. Effect of sodium sulfide on Ni-containing carbon monoxide dehydrogenases. *J. Am. Chem. Soc.* **126**, 9094–9100 (2004).
27. Nakamura, M., Saeki, K. & Takahashi, Y. Hyperproduction of recombinant ferredoxins in *Escherichia coli* by coexpression of the ORF1-ORF2-*iscS-iscU-iscA-hscB-hscA-fdx*-ORF3 gene cluster. *J. Biochem.* **126**, 10–18 (1999).
28. Miller, E., Wohlfarth, G. & Diekert, G. Comparative studies on tetrachloroethene reductive dechlorination mediated by *Desulfitobacterium* sp. strain PCE-S. *Arch. Microbiol.* **168**, 513–519 (1997).
29. Munasinghe, P. C. & Khanal, S. K. Syngas fermentation to biofuel: evaluation of carbon monoxide mass transfer coefficient ($k_L a$) in different reactor configurations. *Biotechnol. Progr.* **26**, 1616–1621 (2010).

30. Yung-Chi, C. & Prusoff, W. H. Relationship between the inhibition constant (K_i) and the concentration of inhibitor which causes 50 percent inhibition (I_{50}) of an enzymatic reaction. *Biochem. Pharmacol.* **22**, 3099–3108 (1973).

31. Otwinowski, Z. & Minor, W. Processing of X-ray diffraction data collected in oscillation mode. *Methods Enzymol.* **276**, 307–326 (1997).

32. Dobbek, H., Svetlitchnyi, V., Liss, J. & Meyer, O. Carbon monoxide induced decomposition of the active site [Ni–4Fe–5S] cluster of CO dehydrogenase. *J. Am. Chem. Soc.* **126**, 5382–5387 (2004).

33. Emsley, P. & Cowtan, K. Coot: model-building tools for molecular graphics. *Acta Crystallogr. D* **60**, 2126–2132 (2004).

34. Liebschner, D. et al. Macromolecular structure determination using X-rays, neutrons and electrons: recent developments in *Phenix. Acta Crystallogr. D* **75**, 861–877 (2019).

35. Winn, M. D. et al. Overview of the CCP4 suite and current developments. *Acta Crystallogr. D* **67**, 235–242 (2011).

36. Brooks, B. R. et al. CHARMM: a program for macromolecular energy, minimization, and dynamics calculations. *J. Comput. Chem.* **4**, 187–217 (1983).

37. Jorgensen, W. L., Chandrasekhar, J., Madura, J. D., Impey, R. W. & Klein, M. L. Comparison of simple potential functions for simulating liquid water. *J. Chem. Phys.* **79**, 926–935 (1983).

38. Darden, T., York, D. & Pedersen, L. Particle mesh Ewald: an $N\log(N)$ method for Ewald sums in large systems. *J. Chem. Phys.* **98**, 10089–10092 (1993).

39. Ryckaert, J.-P., Ciccotti, G. & Berendsen, H. J. C. Numerical integration of the Cartesian equations of motion of a system with constraints: molecular dynamics of *n*-alkanes. *J. Comput. Phys.* **23**, 327–341 (1977).

40. DeVane, R. et al. A molecular dynamics method for calculating molecular volume changes appropriate for biomolecular simulation. *Biophys. J.* **85**, 2801–2807 (2003).

41. Zhang, Y. & Skolnick, J. TM-align: a protein structure alignment algorithm based on the TM-score. *Nucleic Acids Res.* **33**, 2302–2309 (2005).

42. Kumar, S., Stecher, G., Li, M., Knyaz, C. & Tamura, K. MEGA X: molecular evolutionary genetics analysis across computing platforms. *Mol. Biol. Evol.* **35**, 1547–1549 (2018).

43. Huerta-Cepas, J. et al. eggNOG 5.0: a hierarchical, functionally and phylogenetically annotated orthology resource based on 5090 organisms and 2502 viruses. *Nucleic Acids Res.* **47**, D309–D314 (2019).

Author contributions

Y.H.K. and S.M.K. conceived and planned all the experiments. S.M.K. performed the bioinformatic analysis and gene cloning. S.M.K. and J.L. performed the biochemical characterization, kinetic analysis and feasibility evaluation, all under the supervision of Y.H.K. S.M.K. and S.H.K. engineered the gas tunnels and performed their structural analysis. Y.H.K., S.M.K. and J.-S.H. wrote the manuscript. H.H.L., H.-J.Y. and Y.H. determined the crystal structure. Y.H.K., H.H.L. and J.-S.H. reviewed the manuscript.

Competing interests

The authors declare no competing interests.

Additional information

Supplementary information The online version contains supplementary material available at https://doi.org/10.1038/s41929-022-00834-y.

Correspondence and requests for materials should be addressed to Hyung Ho Lee or Yong Hwan Kim.

Peer review information *Nature Catalysis* thanks Tristan Wagner, Anna Rovaletti, Stephen Ragsdale and the other, anonymous, reviewer(s) for their contribution to the peer review of this work.

Reprints and permissions information is available at www.nature.com/reprints.

Publisher's note Springer Nature remains neutral with regard to jurisdictional claims in published maps and institutional affiliations.

nature portfolio

Corresponding author(s): Yong Hwan Kim

Last updated by author(s): Jul 26, 2022

Reporting Summary

Nature Portfolio wishes to improve the reproducibility of the work that we publish. This form provides structure for consistency and transparency in reporting. For further information on Nature Portfolio policies, see our Editorial Policies and the Editorial Policy Checklist.

Statistics

For all statistical analyses, confirm that the following items are present in the figure legend, table legend, main text, or Methods section.

n/a	Confirmed	
☐	☒	The exact sample size (n) for each experimental group/condition, given as a discrete number and unit of measurement
☐	☒	A statement on whether measurements were taken from distinct samples or whether the same sample was measured repeatedly
☒	☐	The statistical test(s) used AND whether they are one- or two-sided *Only common tests should be described solely by name; describe more complex techniques in the Methods section.*
☒	☐	A description of all covariates tested
☒	☐	A description of any assumptions or corrections, such as tests of normality and adjustment for multiple comparisons
☐	☒	A full description of the statistical parameters including central tendency (e.g. means) or other basic estimates (e.g. regression coefficient) AND variation (e.g. standard deviation) or associated estimates of uncertainty (e.g. confidence intervals)
☒	☐	For null hypothesis testing, the test statistic (e.g. F, t, r) with confidence intervals, effect sizes, degrees of freedom and P value noted *Give P values as exact values whenever suitable.*
☒	☐	For Bayesian analysis, information on the choice of priors and Markov chain Monte Carlo settings
☒	☐	For hierarchical and complex designs, identification of the appropriate level for tests and full reporting of outcomes
☒	☐	Estimates of effect sizes (e.g. Cohen's d, Pearson's r), indicating how they were calculated

Our web collection on statistics for biologists contains articles on many of the points above.

Software and code

Policy information about availability of computer code

Data collection	Data were collected using the Agilent Technologies Cary WinUV Kinetics Application V.5.0.0.999 and the Agilent Chemstation software Version B.04.03. Crystal Data were collected using the Macromolecular Crystallography Data Collector software (MxDC).
Data analysis	Data were analyzed using SigmaPlot Version 10.0 (10.0.0.54), Agilent Technologies Cary WinUV Kinetics Application V.5.0.0.999, Agilent Chemstation software Version B.04.03, PyMOL Molecular Graphics System Version 2.4.0, CAVER PyMOL 3.0 Plugin, Discovery Studio Client v22.1.0.21297, MEGA Version 10.1.8, TM-align online Server (2021), EggNOG v5.0 online Server, HHKL2000 v721, CCP4i 7.1.018, PHENIX 1.19.2_4158, and Coot 0.9.8.

For manuscripts utilizing custom algorithms or software that are central to the research but not yet described in published literature, software must be made available to editors and reviewers. We strongly encourage code deposition in a community repository (e.g. GitHub). See the Nature Portfolio guidelines for submitting code & software for further information.

Data

Policy information about availability of data

All manuscripts must include a data availability statement. This statement should provide the following information, where applicable:

- Accession codes, unique identifiers, or web links for publicly available datasets
- A description of any restrictions on data availability
- For clinical datasets or third party data, please ensure that the statement adheres to our policy

Structural data that support the findings of this study have been deposited in the Protein Data Bank (PDB) with the accession codes 7ERR (aerobic A559W), 7XDM (anaerobic A559W), 7XDN (anaerobic A559H), and 7XDP (anaerobic A559S). MD trajectories of total 5 nanoseconds are available on Zenodo at https://doi.org/10.5281/zenodo.6865415.

Field-specific reporting

Please select the one below that is the best fit for your research. If you are not sure, read the appropriate sections before making your selection.

☒ Life sciences ☐ Behavioural & social sciences ☐ Ecological, evolutionary & environmental sciences

For a reference copy of the document with all sections, see nature.com/documents/nr-reporting-summary-flat.pdf

Life sciences study design

All studies must disclose on these points even when the disclosure is negative.

Sample size	No statistical methods were used to predetermine the sample size. At least three independent experiments were performed in this work. Sample sizes were determined on the basis of previous experiments by considering biological and technical variabilities.
Data exclusions	No data were excluded in this work
Replication	At least three independent experiments were performed to verify our results. All of the attempts were successful.
Randomization	Randomization was not applicable for the experiments performed, since no statistical comparisons were performed
Blinding	Blinding was not relevant to our study, since no statistical comparisons were performed

Reporting for specific materials, systems and methods

We require information from authors about some types of materials, experimental systems and methods used in many studies. Here, indicate whether each material, system or method listed is relevant to your study. If you are not sure if a list item applies to your research, read the appropriate section before selecting a response.

Materials & experimental systems

n/a	Involved in the study
☒	☐ Antibodies
☒	☐ Eukaryotic cell lines
☒	☐ Palaeontology and archaeology
☒	☐ Animals and other organisms
☒	☐ Human research participants
☒	☐ Clinical data
☒	☐ Dual use research of concern

Methods

n/a	Involved in the study
☒	☐ ChIP-seq
☒	☐ Flow cytometry
☒	☐ MRI-based neuroimaging